doi:10.20944/preprints202208.0113.v1

Liquid Metal-assisted In-situ Control of Temperature Field for Additive Manufacturing of Titanium Alloys

Xiaohan Zhang[a], Min Xia[c], Yaowu Hu[a,b,*]

[a]The Institute of Technological Sciences, Wuhan University, Wuhan, 430072, China
[b]School of Power and Mechanical Engineering, Wuhan University, Wuhan, 430072, China
[c]Department of Engineering, Lancaster University, Lancaster, LA1 4YW, United Kingdom
*Corresponding author: Yaowu Hu
E-mail: yaowuhu@whu.edu.cn

Abstract

How to effectively suppress thermal cracks in the metal laser additive manufacturing process is still one of the key issues to be solved in the field of laser additive manufacturing. Metal tin, with wide liquid phase working temperature range, high boiling point, low viscosity, high thermal conductivity and excellent electrical conductivity. The use of tin as an auxiliary thermal management material in the metal additive manufacturing process is expected to achieve effective regulation of the temperature field and stress field of the formed part, thereby inhibiting the initiation of cracks and obtaining formed parts with the target grain structure and high reliability. This paper presented a novel liquid metal-assisted laser additive manufacturing method (LMAAM). A numerical model for the laser additive manufacturing of tin-assisted titanium alloys was established. The differences of the flow field, temperature field and stress field of the formed parts with tin and without tin were compared and analyzed. The influence of the interaction position between the tin liquid level and the forming part on the temperature field and stress field of the forming part was deeply studied. The laser additive manufacturing experiment of tin-assisted titanium alloy was carried out, and the experimental results were basically consistent with the simulation results, which verified the validity of the model. LMAAM technology has proven to be an effective method for additive manufacturing of highly reliable formed parts.

Key words: Liquid metal; Additive manufacturing; Thermal management; Temperature gradient; Cooling rate; Crack

1. Introduction

The traditional machining metal subtractive manufacturing technology often has the drawback of a large waste of material resources. Metal material preparation processes such as powder metallurgy and investment casting also often correspond to complicated procedures, high mold costs and time costs. In addition, when small batches of complex precision components are produced, the manufacturing process is required to have high flexibility characteristics. The laser additive manufacturing process is a new type of manufacturing technology that uses a high-power density laser beam to melt metal powder or wire, and prepares a structural shaped part with a special size on the surface of the substrate. This technology has many advantages such as high manufacturing efficiency, high forming accuracy, high material utilization rate and high flexibility[1–3]. Laser additive manufacturing technology is considered to be an efficient process technology for the preparation of new dynamic precision and complex structural parts, and is gradually applied in aerospace, locomotive manufacturing, marine ships and military industries[4–6].

However, the cracking of the formed parts in the metal additive manufacturing process has become the Achilles' heel that restricts the further development and application of the laser additive manufacturing process[7,8]. In the additive manufacturing process, when the high-energy heat source interacts with the material, under the action of the temperature difference, the heat flow spreads along the thickness direction of the formed part. There is bound to be an obvious temperature gradient distribution in each part of the formed part. The temperature gradient is closely related to the microstructure and mechanical properties of the material: on the one hand, an excessive temperature gradient reduces the uniformity of the grain size in the thickness direction of the material and increases the anisotropy of the material[9]. On the other hand, when the material undergoes cold plastic deformation, uneven deformation occurs between grains or between subgrains within grains, which induces microscopic internal stress. When the material is subjected to external loads at the same time, micro-cracks are prone to occur inside the material[10]. Therefore, how to control the temperature field of the formed parts in the laser additive manufacturing process more effectively in real time, and finally obtain the formed parts with the target performance, is undoubtedly an important problem that needs to be solved urgently in the field of metal additive manufacturing at this stage.

At present, researchers in the field have carried out some research work on the regulation of the temperature field and stress field of materials in the additive manufacturing process. Optimizing the process parameters of laser additive manufacturing to achieve thermal regulation of materials is a widely used method. For example, G.Vastola et al.[11] established a numerical model for electron beam additive manufacturing of Ti6Al4V based on the idea of finite element. The effects of electron beam size, power density, scanning speed and preheating temperature on the heat-affected zone and residual stress of the formed parts were studied. T. Mukherjee et al.[12] established a thermal-fluid-mechanical coupling numerical model for laser additive manufacturing of Inconel718 and Ti6Al4V alloys. The stress-strain evolution process of materials in additive manufacturing and its relationship with process parameters such as heat input and monolayer deposition thickness were studied. Based on the ABAQUS simulation software, Li et al.[13] studied the temperature field, residual stress field and deformation of the formed parts under different deposition path strategies, and proposed the optimal deposition path strategy. Levkulich et al.[14] investigated the effect of laser powder bed melting process parameters (scanning speed, laser power, forming height, forming plane area, and substrate conditions) on residual stress and deformation. The above simulation and experimental work show that the process parameters have a great influence on the temperature and stress distribution of the material.

The use of auxiliary processes to thermally control the formed parts of additive manufacturing has gradually become a research hotspot in recent years due to the reduction of trial and error in adjusting process parameters, and the control effect is obvious. According to the real-time sequence of auxiliary process, it can be divided into post-processing method and in-situ method. The post-processing methods such as heat treatment[15], laser remelting[16], laser shock[17], and rolling[18] can be used to improve the stress distribution inside the material. The use of the above post-processing methods to control the stress of the formed parts has the disadvantage of being time-consuming and labor-intensive. In the process of additive manufacturing, the simultaneous implementation of auxiliary processing methods can control the solidification behavior and heat and mass transfer process of the molten pool in real time, so as to control the thermal distribution of materials more effectively. Common in-situ methods include auxiliary heating, ultrasonic shock, strong convection heat dissipation, and external magnetic field. John D. Roehling et al.[19] used shaping light to irradiate the surface of the additively manufactured stainless steel material, controlled the surface temperature of the material, and implemented an in-situ annealing treatment to reduce the harmful residual stress of the formed part. Shen et al.[20] used induction heating to improve the stress distribution of WAAM parts by performing localized in-situ heat treatment on the part surface. The results showed that localized induction heating enabled effective regulation of the stress of additively manufactured parts. Wei et al.[21] applied in-situ ultrasonic shock to additive manufacturing and investigated the effects of ultrasonic shock treatment on the flow behavior, heat transfer behavior, and solidification conditions at the solidification boundary of the molten pool. The results showed that with the increase of ultrasonic power, the temperature gradient of the molten pool first decreased and then increased, and the solidification rate first increased and then decreased. William Hackenhaar et al.[22] studied the temperature field distribution of materials under two different cooling methods, free convection and air jet impingement, in the process of arc additive manufacturing. The results showed that by using air jet cooling and optimizing the interlayer residence time, the convective heat transfer rate of the material could be significantly increased, the heat input in the additive manufacturing process could be controlled, and the risk probability of coating peeling failure could be reduced. Nie et al.[23] introduced a transverse static magnetic field during laser remelting of inconel718 superalloy to study its effect on residual stress and microstructural changes. The results showed that the applied magnetic field could effectively reduce the residual stress during the rapid solidification of 718 superalloy by laser remelting.

Magical liquid metal materials, that is, metals or their alloys with a melting point below 300 ℃, including metal tin, metal gallium, gallium-indium alloys, and gallium-indium-tin alloys. Liquid metal has a wide liquid phase operating temperature range, high boiling point, high density, low viscosity, high thermal conductivity and excellent electrical conductivity[24,25]. At present, liquid metal has been used in the heat dissipation of the core structural parts (such as chips) of electronic devices[26,27] and the field of casting[28,29]. The use of liquid metal as an auxiliary thermal management material in the additive manufacturing process is expected to improve the real-time regulation of the temperature field of the formed parts in the metal additive manufacturing process, and has extremely high engineering application prospects.

In this work, a liquid metal-assisted laser additive manufacturing method was proposed, and tin was used as an auxiliary thermal management material for the additive manufacturing of titanium alloy laser fuses to control the cooling rate and residual stress of the samples. A numerical model for tin-assisted laser additive manufacturing of titanium alloys was established. The differences in flow field, and temperature field and stress field of tin-containing and tin-free parts were compared and analyzed. The influence of the interaction position between the tin level and the forming part on the temperature field and stress field of the forming part was deeply studied. At the same time, the experiment of tin-assisted laser additive manufacturing of titanium alloy was carried out. Simulation and experimental results verify that LMAAM technology was an effective additive manufacturing method for highly reliable molded parts. This research is expected to further promote the development of additive manufacturing technology and provide advanced data reference and theoretical guidance for additive manufacturing of high-reliability structural parts.

2. Experimental

2.1 Experiment and material details

Fig. 1 showed the schematic diagram of the LMAAM process and a high-speed camera image. This work adopted the laser melting wire additive process. The substrate was selected from Ti6Al4V (TC4) alloy, and the elements of the material were as shown in **Table 1**. Sandpaper (240 mesh, 400 mesh, 1500 mesh, 2000 mesh, 3000 mesh) and diamond spray grinding and polishing agent (W0.5, W0.25, W0.1) were used to pre-polish the substrate. Anhydrous ethanol and an ultrasonic cleaner were used to clean the substrate. The wire material was Ti6Al4V (TC4) alloy with a diameter of 1.2 mm.. The elements of the wire material were as shown in **Table 2**. The auxiliary thermal management material was metal tin with a purity of 99.99% (melting point was 231.89 ℃, boiling point was 2260 ℃). The experimental research was carried out using the MFSC-1000X single-mode continuous fiber laser produced by Shenzhen Maxphotonics Laser Co., Ltd. The three-coordinate moving platform was used to control the path of laser scanning. The specific process parameters of the LMAAM process were shown in **Table 3**.

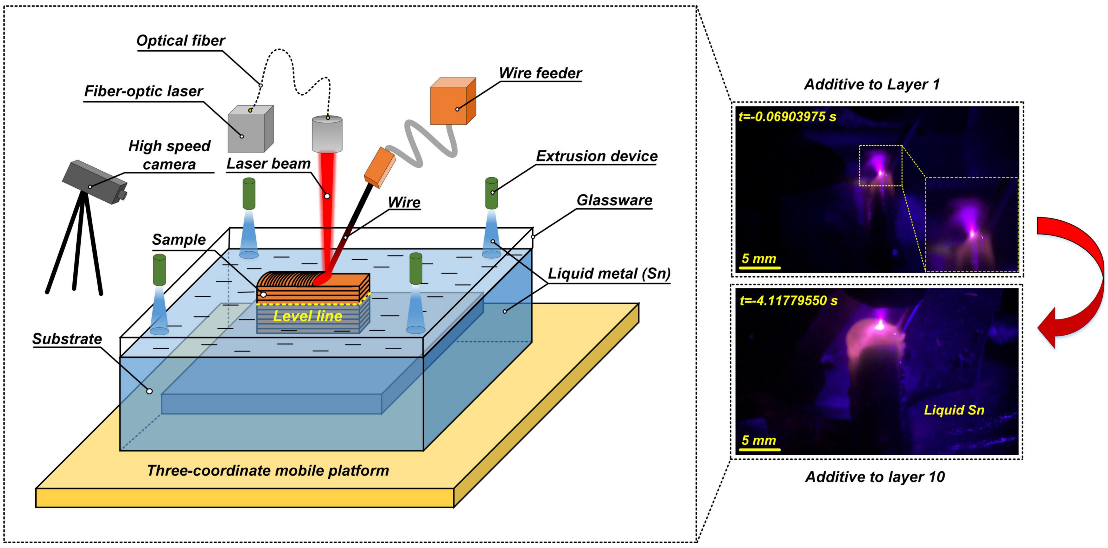

Fig. 1 Schematic diagram of the LMAAM process and a high-speed camera image

Table. 1 Main element composition of the titanium alloy substrate

Element	Fe	C	N	H	O	V	Al	Ti
Content(*wt*%)	0.30	0.10	0.05	0.015	0.20	3.5-4.5	5.5-6.8	Bal

Table. 2 Main element composition of the titanium alloys wire

Element	Fe	C	N	H	O	V	Al	Ti
Content(*wt*%)	0.20	0.07	0.02	0.010	0.12	4.0	5.9	Bal

Table. 3 Process parameters of LMAAM

Process parameters	value
Laser power/W	400
Laser duty cycle	100%
Laser frequency/Hz	5000
Ramp up time/ms	200
Galvo speed/Hz	80
Width of galvanometer/mm	1
Wire feeding speed/mm·s^{-1}	20
Shielding gas (Ar) flow/MPa	1.25
Laser scanning speed/mm·s^{-1}	2
Thermal management material (Sn) initial temperature/K	523

2.2. Experimental equipment and characterization methods

The metallographic microscope (BX53M, Olympus Inc., Japan) was used to observe the macroscopic appearance of titanium alloys. A high-speed camera (Phantom, V1612, USA) matched with a miniature zoom lens (Navitar 12-X) was used to film the LMAAM process. XRD (X' Pert PRO, Almelo, Netherlands) was performed to investigate the phase structure and crystal orientation of samples produced by different processing methods. The scan was performed using Cu Kα1 radiation (λ=0.1541 nm) at the 2θ range from 20° to 90°, the measurement time was 0.2 s, the non-width angle was 0.04°, the tube voltage was 40 V, and the tube current was 40 A. The integrated patterns were then analyzed using Jade 6 for phase identification. The field emission scanning electron microscope (MIRA 3, TESCAN Brno,s.r.o. Inc., Czech Republic) with electron back-scattered diffraction(EBSD) (Aztec HKL standard, Oxford Instruments Nanoanalysis Inc., U.K) was used to observe the morphology of the grains and count the size of the grains. The micro vickers hardness tester (FM-800, Future-Tech Inc., Japan) was used to test the microhardness of samples.

3. Simulation

3.1 Local flow field simulation

The numerical model of LMAAM was established based on Flow-3D software. The computational domain was set to uniform grid cells. Boundary conditions that approximate the experimental conditions were imposed on the computational domain. The upper surface is set as the pressure boundary condition, the surrounding surface is set as the outflow boundary condition, and the lower surface was set as the wall boundary condition. As shown in **Fig. 2**, the modeling method of the symmetrical model was adopted, and the size of the model on one side was 20 mm × 7 mm × 10 mm. The grid size was 0.25 mm. Void region and Fluid region represented the atmospheric environment and the additive material, respectively. The calculation and reconstruction of the free surface in the additive was carried out using implicit SOR and VOF algorithms. The update of the free surface was achieved by adding the heat source and driving models to the governing equations in each iteration through Fortran language subroutines. Boundary conditions would be applied on all meshes until the end of computation time.

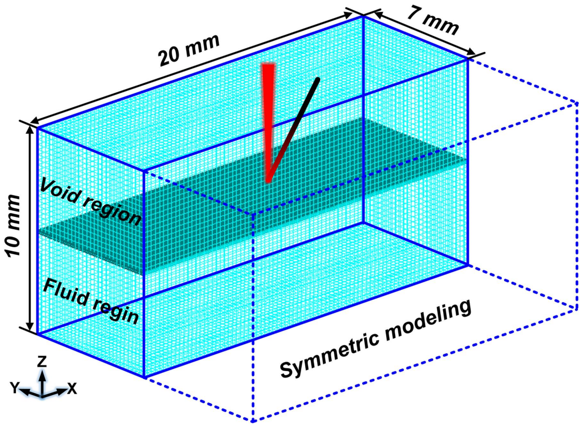

Fig. 2 Finite element model of the LMAAM process in the simulation

1) Conservation equation

In this calculation model, the velocity fields and temperature fields of the solid and liquid phases were calculated using the following mass (Eq. 1), momentum (Eq. 2) and energy (Eq. 3) conservation equations[30].

$$\frac{\partial}{\partial t}(\rho)+\nabla(\rho\vec{V})=0 \tag{1}$$

$$\frac{\partial}{\partial t}(\rho\vec{V})+\nabla(\rho\vec{V}\vec{V})=\nabla(\mu\nabla\vec{V})\text{-}\nabla P-\frac{\mu}{K}\vec{V}+\rho g \tag{2}$$

$$\frac{\partial}{\partial t}(\rho h)+\nabla(\rho\vec{V}h)=\nabla(K\nabla T) \tag{3}$$

In Eq. 1, ρ was the density and V is the velocity. In Eq. 2, μ was the fluid viscosity, P was the pressure, K was the isotropic permeability expressed by the Kozeny-Carman equation, and g was the gravity. The last two terms on the right side of the Eq. 2 represented the source terms for the liquid phase damping force and gravity, respectively. In Eq. 3, T was the temperature, h was the material enthalpy, and k was the thermal conductivity.This work adopted the laser melting wire additive process.

2) Force equation

The driving force of molten pool flow, in addition to the gravity considered above, this paper also considered the influence of surface tension, Marangoni effect and metal evaporation and its recoil pressure on molten pool flow. During the calculation, the surface tension was reduced to the equivalently acting pressure on the free surface, as shown in Eq. 4.

$$P_S=\frac{\sigma_S}{r} \tag{4}$$

Where: r was the curvature radius of the free surface. σ_s was the surface tension coefficient. During the calculation, the set surface tension coefficient and temperature were linear, as shown in Eq. 5.

$$\sigma_s=\sigma_{s0}-\sigma_s^T(T-T_0) \tag{5}$$

where: σ_{s0} was the surface tension coefficient at the reference temperature(T_0). σ_s^T was the coefficient of surface tension variation with temperature.

The temperature gradient would cause the gradient of surface tension, which drived the liquid to flow, which was the Marangoni effect. When the input energy density was high, the steam recoil pressure (Eq. 6) replaced the Marangoni effect as the main driving force of the molten pool flow[31,32].

$$P_r = 0.54P_0 \exp\left(\Delta H_{LV}\frac{T-T_{LV}}{RTT_{LV}}\right) \tag{6}$$

In the formula: P_r was the boiling point vapor pressure. T_{LV} was the boiling point temperature. ΔH_{LV} was the effective enthalpy of metal vaporization.

3.2 Multilayer temperature field simulation

With the help of the finite element simulation software, based on the method of life and death elements, using the APDL parameterization language, a numerical model of LMAAM was established. Before the calculation starts, the entire additive process was discretized into multiple units, and all the coating units were killed. With the progress of the additive process, the additive units were gradually activated until the entire additive process ends. **Fig. 3** showed a the finite element model of the LMAAM process. The structural parameters of the substrate (TC4) were 40×40×5 mm, and the structural parameters of the coating (TC4) were 40×4×0.8 mm. The thermal management material was tin metal. Numerical calculations were carried out using a SOLID70 hexahedral eight-node body element. In order to improve the accuracy of simulation calculation and simultaneously improve the efficiency of simulation calculation, the model was divided into regions and meshed. The dimensions of the coating elements (green) were 0.4 mm. The perimeter of the coating, that was, the substrate area elements (red) adjacent to the coating and the pure tin metal area unit (purple) adjacent to the coating were 0.8 mm in size. The dimensions of the elements in other areas are 1 mm. The temperature field and residual stress field distribution of the sample were studied when the distance between the tin liquid level and the top of the molded part was 0 mm(case1), 0.8 mm(case2), 1.6mm(case3), 2.4 mm(case4), 3.2 mm(case5) and 4 mm (case6). Since it was difficult to consider all factors of the experimental process in the simulation, in order to improve the calculation efficiency, the model needed to be simplified and reasonable assumptions should be made during the simulation calculation of temperature field: 1) The material was an isotropic and uniform medium; 2) The flow of the molten pool was ignored, and the convective heat transfer caused by the fluid flow in the molten pool was simulated by increasing the thermal conductivity of the material by 2 times in the liquid phase[33]; 3) The residual height generated on the surface of the material during the actual laser additive remanufacturing process was ignored, that was, it was assumed that the surface of the additively manufactured material was a regular plane.

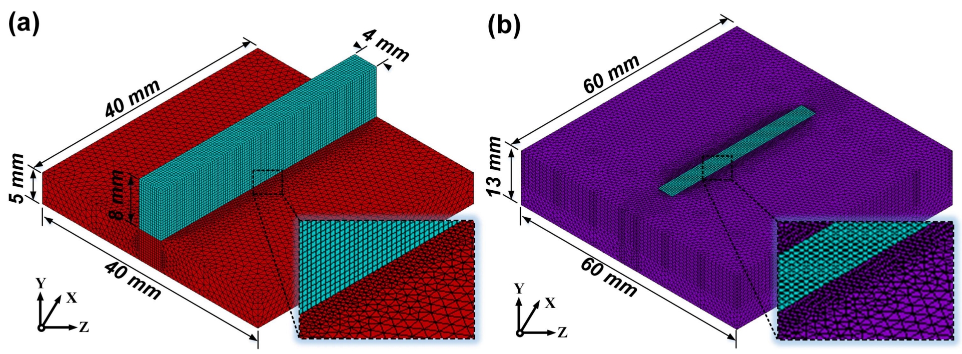

Fig. 3 Finite element model of the LMAAM process in the simulation

(1) Heat transfer constitutive model

The interaction process between laser heat source and material was a complex three-dimensional transient heat transfer process, and the corresponding transient heat transfer differential equation for this process was shown as Eq. 7[34]:

$$c\rho\frac{\partial T}{\partial t}=\frac{\partial}{\partial x}(\lambda\frac{\partial T}{\partial x})+\frac{\partial}{\partial y}(\lambda\frac{\partial T}{\partial y})+\frac{\partial}{\partial z}(\lambda\frac{\partial T}{\partial z})+Q \tag{7}$$

Where c was the specific heat capacity; ρ was the density; λ was the thermal conductivity; T was the temperature; Q was the internal heat source (including the energy of the laser photon and the heat released by the phase transition); t was the heat transfer time. Where c, ρ, and λ are all functions of temperature. In order to solve the heat conduction equation, initial conditions and boundary conditions needed to be set.

(2) Initial conditions

At the start of the laser additive operation (operation time t=0), the substrate and Sn had a uniform initial temperature, namely as Eq. 8:

$$T(x,y,z,t)\big|_{t=0}=T_0 \tag{8}$$

In the formula: T_0 was the initial temperature of the material, where the initial temperature of the substrate was 25 °C, and the initial temperature of the Sn thermal management material was 250 °C.

(3) Boundary conditions

Laser as a heat source, the consideration of the heat source model was an important link in the numerical simulation. According to the wave-particle duality of the laser and the characteristics of the interaction between the laser and the material, during the laser additive process, since the material was melted, the bulk heat source model was used for loading. The LMAAM simulation process parameters were: the laser power was 300 W, the laser scanning speed was 5 mm/s, the spot radius was 2 mm, and the absorption rate as 0.27. Whether the selection of the laser heat source model was suitable or not would have a great influence on the calculation accuracy of the subsequent temperature field and stress field. In this paper, the Gaussian cone heat source model was selected. The heat flow was mainly concentrated in the center of the heat source and gradually decreased along the edges. The central heat flow in the depth direction of the heat source did not change. The radius of the heat source varied linearly along the depth of the material. The distribution equation of the heat source was shown in Eq. 9-10[35]:

$$q_m(x,y,z)=\frac{9Q_0}{\pi\left(1-e^{-3}\right)\left(Z_e-Z_i\right)\left(r_e^2+r_er_i+r_i^2\right)}\exp(-3\,\frac{x^2+y^2}{r_0^2(z)}) \tag{9}$$

$$r_0(z)=r_e+(r_e-r_i)\frac{Z-Z_e}{Z_e-Z_i} \tag{10}$$

where re and ri were the upper and lower opening radii of the cone heat source, respectively. $Q_0=\eta P$ was the net heat input. η was the laser energy absorption rate. P was the laser power. r_0 was the heat distribution coefficient. The heat flux density distribution in the area where the material directly interacts with the laser was shown as Eq. 11:

$$\lambda\frac{\partial T}{\partial x}n_x+\lambda\frac{\partial T}{\partial y}n_y+\lambda\frac{\partial T}{\partial z}n_z=q_m(x,y,z,t) \tag{11}$$

Since the heat flux density and convective heat transfer coefficient of the laser could not be loaded on the same unit at the same time, the SURF152 surface effect unit was used, and the convective heat transfer between the material and the external environment was loaded through steady-state calculation. During the laser additive process, the surface of the sample in contact with the air dissipates heat to the surrounding environment mainly through convection and radiation, that was, the third type of boundary condition. If the convection and radiation are calculated separately, the nonlinearity of the temperature field would be increased, and the convergence of the calculation process would be reduced. In order to improve the convergence, this paper considered the combination of two heat transfer modes, convection and radiation, that was, a total heat transfer coefficient h, including heat convection and heat radiation[36]. The heat exchange between the boundary of an object and the surrounding environment could be expressed by the following Eq. 12:

$$\lambda\frac{\partial T}{\partial x}n_x+\lambda\frac{\partial T}{\partial y}n_y+\lambda\frac{\partial T}{\partial z}n_z=h(T_s-T_a) \tag{12}$$

Where: h was the convective heat transfer coefficient; T_a was the temperature of the environment; T_s was the temperature of the material surface; n_x, n_y, and n_z were the direction cosines of the normal line outside the boundary. When the laser heat source irradiated the material, the material would release latent heat due to phase change, and this heat would affect the cooling time and microstructure of the formed part to a certain extent, so it needed to be considered. Here, the latent heat of phase transition of materials in the additive manufacturing process was considered using the equivalent specific heat capacity method and the enthalpy method, and it could be expressed by the following Eq. 13[37]:

$$H(T)=\int_0^T\rho c(t)\mathrm{d}t \tag{13}$$

In the formula: H was the enthalpy value; ρ was the density of the material.

3.3 Stress field simulation

The stress field of laser additive manufacturing was established based on the thermo-elastic-plastic theory. The finite element method was used to gradually track the temperature change of the additive manufacturing process to calculate the thermal stress and deformation. Because of the complexity of the stress changes in this process, appropriate simplifications were required when performing a thermo-elastoplastic analysis. The assumptions were as follows: 1) Plastic deformation did not cause volume change, that was, the law of volume invariance was satisfied. 2) The plastic deformation satisfied the law of constant volume; 3) The deformation process of the material followed the Von Mises yield criterion; 4) In the plastic deformation zone, the deformation of the material followed the plastic flow criterion and the follow-up strengthening criterion; 5) When the time interval was small, the thermal stress and strain of the material and related mechanical properties parameters were considered to change linearly; 6) The effects of viscosity and creep were not considered; 7) All materials were isotropic.

(1) Thermo-elastoplastic constitutive model

In the process of additive manufacturing, as the temperature increases, the elastic modulus and thermal expansion coefficient of the material increased, while the yield limit decreased with the increase of temperature, and the material gradually approaches the ideal plastic material. The total strain of the material could be represented by Eq. 14.

$$d\{\varepsilon\}=d\{\varepsilon_e\}+d\{\varepsilon_P\}+d\{\varepsilon_T\} \tag{14}$$

where $d\{\varepsilon_e\}$ was the elastic strain increment, $d\{\varepsilon_p\}$ was the plastic strain increment, and $d\{\varepsilon_T\}$ was the thermal strain increment.

1) Elastic strain increment

According to the generalized Hooke's law, the elastic strain increment could be expressed as Eq. 15:

$$d\{\sigma\}=[D_e]d\{\varepsilon_e\} \tag{15}$$

where $[D_e]$ was the elastic matrix, which was the coefficient matrix related to the elastic modulus E and Poisson's ratio μ, and changed with temperature T. Therefore, the elastic strain increment could be represented by Eq. 16:

$$d\{\varepsilon_e\}=[D_e]^{-1}d\{\sigma\}+\frac{[D_e]^{-1}}{\partial T}\{\sigma\}dT \tag{16}$$

2) Plastic strain increment

Under the conditions of temperature T, strain hardening index K, etc., when the material yield function $f(\sigma_x,\sigma_y,...)$ reached $f(\sigma_s,T,K)$, the material began to yield. According to the flow criterion, the material plastic strain increment could be represented by Eq. 17:

$$d\{\varepsilon_p\}=\lambda\frac{\partial f}{\partial\{\alpha\}} \tag{17}$$

where f was the yield function, which was a function of stress state and plastic strain. α was the thermal expansion coefficient.

3) Thermal strain increment

The thermal strain increment could be expressed as Eq. 18:

$$d\{\varepsilon_T\}=\{\alpha_0 dT+Td\alpha_0\}=\left\{\alpha_0+\frac{\partial\alpha_0}{\partial T}d\alpha_0\right\}dT=\{\alpha\}dT \tag{18}$$

4) Stress-strain relationship

①Elastic zone

Since there was no plastic strain in the elastic region, the increment of the total strain could be expressed as Eq. 19:

$$d\{\varepsilon\}=d\{\varepsilon_e\}+d\{\varepsilon_T\} \tag{19}$$

After substituting the expressions for elastic strain and thermal strain into Eq. 19, Eq. 20-21 could be obtained. Finally, the incremental constitutive equation of the elastic region was obtained, and it could be expressed as Eq. 22.

$$d\{\sigma\}=[D_e]d\{\varepsilon\}-\left\{[D_e]\{\alpha\}+\frac{\{\sigma\}}{\partial T}\right\}dT \tag{20}$$

$$\{C_e\}=\left\{[D_e]\{\alpha\}+\frac{\{\sigma\}}{\partial T}\right\} \tag{21}$$

$$d\{\sigma\}=[D_e]d\{\varepsilon\}-\{C_e\}dT \tag{22}$$

①Plastic zone

In the plastic zone, the total strain increment was expressed as Eq. 23-26:

$$d\{\sigma\}=\left[D_{ep}\right]d\{\varepsilon\}-\left\{\left[D_{ep}\right]\{\alpha\}+\left[D_{ep}\right]\frac{\partial[D_e]^{-1}}{\partial T}-\frac{[D_e]\left[\frac{\partial f}{\partial\sigma}\right]\left[\frac{\partial f_0}{\partial\sigma}\right]}{S}\right\}dT \tag{23}$$

$$S=\left[\frac{\partial f}{\partial\sigma}\right][D_e]\left[\frac{\partial f}{\partial\sigma}\right]+\left[\frac{\partial f_0}{\partial K}\right]\left[\frac{\partial K}{\partial\varepsilon_P}\right]^T\left[\frac{\partial f}{\partial\sigma}\right] \tag{24}$$

$$\left[D_{ep}\right]=[D_e]-\frac{[D_e]\left[\frac{\partial f}{\partial\sigma}\right]\left[\frac{\partial f_0}{\partial\sigma}\right]}{S} \tag{25}$$

$$\left\{C_{ep}\right\}=\left\{\left[D_{ep}\right]\{\alpha\}+\left[D_{ep}\right]\frac{\partial[D_e]^{-1}}{\partial T}-\frac{[D_e]\left[\frac{\partial f}{\partial\sigma}\right]\left[\frac{\partial f_0}{\partial\sigma}\right]}{S}\right\} \tag{26}$$

Finally, the constitutive equation of the plastic zone could be simplified to Eq. 27:

$$d\{\sigma\}=\left[D_{ep}\right]d\{\varepsilon\}-\left\{C_{ep}\right\}dT \tag{27}$$

(2) Initial and Boundary Conditions

Before the start of the additive operation, the entire sample was in a stress-free state. During the entire operation, the displacement of the bottom surface of the sample in the thickness direction was constrained.

3.3. Thermophysical properties of materials

Table. 4 showed the simulation calculation parameters of the TC4 applied in the simulation. **Table. 5** showed the simulation calculation parameters of the TC4 applied in the simulation. **Table. 6** showed the simulation calculation parameters of the Sn applied in the simulation. In order to improve the accuracy of the simulation calculation of stress field, in the numerical simulation, the changes of the thermophysical performance parameters of the TC4 titanium alloy material and the Sn material with the temperature were considered. The melting point of TC4 titanium alloy ranged from 1600 ℃ to 1700 ℃, and the melting point of Sn was 250 ℃. The high temperature thermophysical parameters above the melting point of the material were obtained by the method of difference and extrapolation. When the material temperature rose to the melting point, the material no longer belonged to the elastic deformation range, and the mechanical properties such as elastic modulus and yield strength of the material have lost their physical connotation. By setting the zero stress temperature, we considered the performance of the material's mechanical properties when the material temperature reached its melting point.

Table. 4 Simulation calculation parameters of the TC4 applied in the simulation

Density/kg·m^{-3}	4420
Viscosity/kg·m^{-1}·s^{-1}	0.00325
Specific heat/J·kg^{-1}·K^{-1}	546
Thermal conductivity/W·m^{-1}·K^{-1}	7
Liquidus temperature/K	1925
Solidus temperature/K	1875
Latent heat of fusion	2.86e5
Surface tension coefficient/kg·s^{2}	1.5
Temperature coefficient of surface tension/N·m^{-1}·K^{-1}	4E-4
Ambient temperature/K	300

Table. 5 Simulation calculation parameters of the TC4 applied in the simulation

Temperature /K	**Heat conductivity coefficient /W·m^{-1}·K^{-1}**	**Specific heat capacity /J·kg^{-1}·K^{-1}**	**Density /kg·m^{-3}**	**Elastic modulus /GPa**	**Thermal expansion coefficient /10^{-6}·K^{-1}**	**Yield strength /MPa**	**Poisson's ratio**
300	6.8	611	4510	216	10.4	482	0.337
675	9.9	670	4510	194	11.6	446	0.337
875	12.8	705	4510	166	12.4	364	0.337
1275	15.8	751	4510	96	13.4	138	0.337
1675	24.3	783	4510	52	14.4	100	0.337

Table 6 Simulation calculation parameters of the Sn applied in the simulation

Temperature /K	**Heat conductivity coefficient /W·m^{-1}·K^{-1}**	**Specific heat capacity /J·kg^{-1}·K^{-1}**	**Density /kg·m^{-3}**	**Elastic modulus /GPa**	**Thermal expansion coefficient /10^{-6}·K^{-1}**	**Yield strength /MPa**	**Poisson's ratio**
300	63.2	213	5765	41.6	23.1	90	0.43
675	88	236	5765	36.1	23.6	30	0.43
875	105	266	5765	29.8	24.1	15	0.43
1275	105	288	5765	26.2	24.5	13	0.43
1675	105	302	5765	16	26.4	12	0.43

4. Simulation results and discussion

4.1. Flow field analysis

Fig. 4 showed the cloud diagram of the transient temperature field and flow field of samples under different process conditions. After the interaction between the laser and the material, the samples produced under different process conditions showed obvious temperature gradient distribution. Observing and comparing Fig. 4(a) with Fig. 4(b), Fig. 4(c) with Fig. 4(d), it was found that the sample without tin has a higher peak temperature than the sample with tin. The difference in peak temperature was attributed to the excellent heat transfer properties of tin. Observing and comparing Fig. 4(e) with Fig. 4(f), it was found that the speed of the sample without tin was lower than that of the sample with tin. The difference in the velocity field was attributed to the addition of tin accelerated the heat exchange between the sample and the external environment, reduced the cooling rate of the sample, and accelerated the heat and mass transfer inside the molten pool. In order to further analyze the influence of Sn addition on the temperature field and stress field of the sample during the additive manufacturing process, we carried out advanced research with the help of the simulation finite element simulation software.

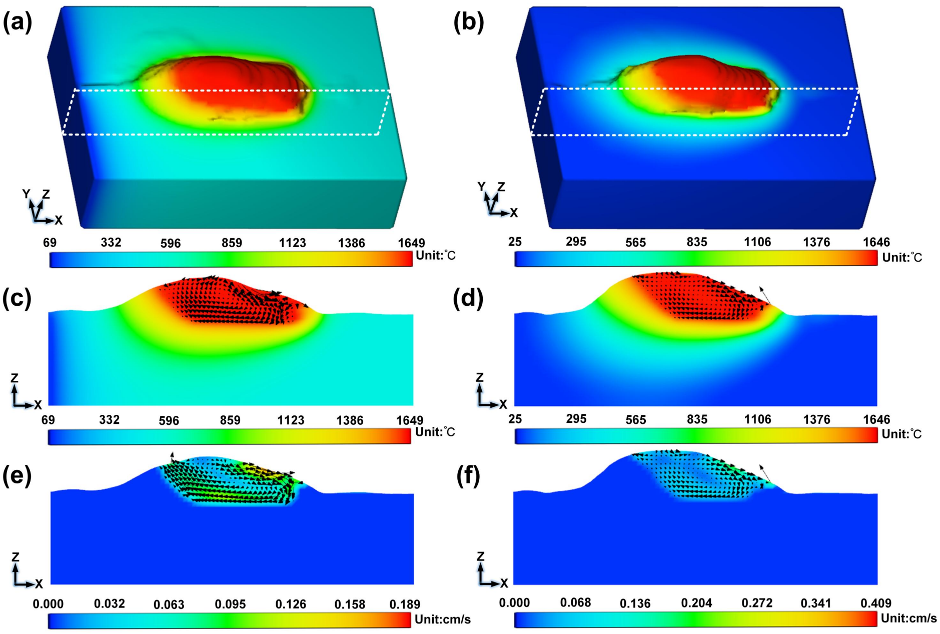

Fig. 4 Cloud diagram of the transient temperature field and flow field of samples under different process conditions: (a) Without Sn/temperature field, (b) With Sn/temperature field,(c) Without Sn/cross-sectional view of temperature field,(d) With Sn/cross-sectional view of temperature field,(e) Without Sn/cross-sectional view of velocity field,(f) With Sn/cross-sectional view of velocity field.

4.2. Temperature field analysis

Fig. 5 showed the cloud diagram of the transient temperature field distribution of LMAAM. The temperature of the area where the sample directly interacted with the laser heat source was high, and the temperature of other areas was low, and the entire sample presented a clear temperature gradient distribution. When the laser interacted with the sample, under the combined effect of the thermal conductivity of the sample and the convective heat transfer with the external environment, the heat diffused from the high temperature area to the low temperature area, which made the temperature field distribution of each part of the sample different. Compared with the peak temperature of the sample without tin, the peak temperature of the sample with tin-assisted thermal management was reduced, which was attributed to the high thermal conductivity of tin, which intensified the heat exchange. With the increase of the distance between the tin liquid level and the top of the sample, the peak temperature of the sample increased gradually. With tin-assisted additive, the heat transfer mechanism differed between the areas of the specimen in direct contact with tin and those not in contact with tin. In the sample area that was not in contact with tin, there was convective heat transfer between the sample and the air and thermal conductivity of the sample itself. In the sample area that was in direct contact with tin, there was more sufficient thermal conductivity, convection heat transfer between the sample and tin, and thermal conductivity of the sample itself. As the distance between the tin liquid level and the top of the sample increased, the actual bonding area between the tin and the sample decreased, the heat transfer energy of the sample weakened, the heat accumulation of the sample itself increased gradually, and the peak temperature of the sample increased gradually.

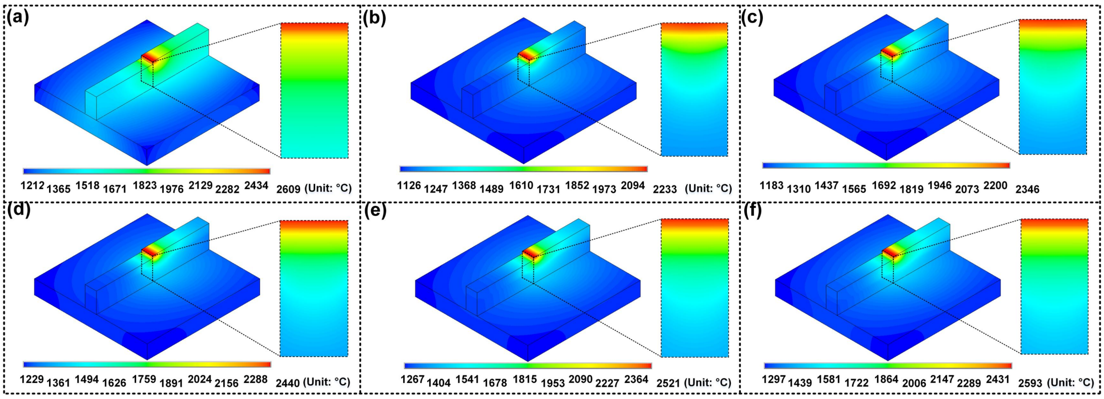

Fig. 5 Cloud diagram of the transient temperature field distribution of LMAAM: (a) case1, (b) case2,(c) case3,(d) case4,(e) case5,(f) case5.

Fig. 6 showed the cloud map of the transient molten pool morphology of the LMAAM sample. The molten pool formed by the laser additive process was "spoon-shaped", and the molten pool area presented a distinct distribution of temperature gradients, that was, the temperature in the area directly irradiated by the heat source was high, and the temperature in the area directly irradiated by the non-heat source was low. In the process of laser additive, the laser moved dynamically, which led to the process of the interaction between the laser and the material to form a molten pool, which was a dynamic process of the formation of a new molten pool and the condensation and annihilation of the old molten pool. Due to the differences in the spatial temperature distribution and cooling rate of the molten pool, the molten pool presented a "spoon-shaped" characteristic morphology. The size of the molten pool of the sample without tin was larger, while the size of the molten pool of the sample with tin was smaller, and the molten pool of the sample increased gradually with the increase of the distance between tin and the top of the sample. There was a close relationship between the size of the molten pool and the heat transfer of the sample itself. When the heat source interacted with the material, if the heat exchange of the sample itself was insufficient, heat would accumulate, and the size of the molten pool of the corresponding sample would be larger. On the contrary, if the heat exchange of the sample itself was sufficient, the heat was difficult to accumulate inside the sample, and the size of the molten pool corresponding to the sample was small. There was no doubt that the excellent heat transfer properties of tin made the peak temperature of the samples with tin lower than that of the samples without tin. The heat accumulation of the sample itself was less, the sample material above the melting point was less, and the characteristic molten pool size was smaller. As the distance between the tin liquid level and the top of the sample increased, the heat accumulation of the sample itself increased, so the size of the molten pool increased gradually.

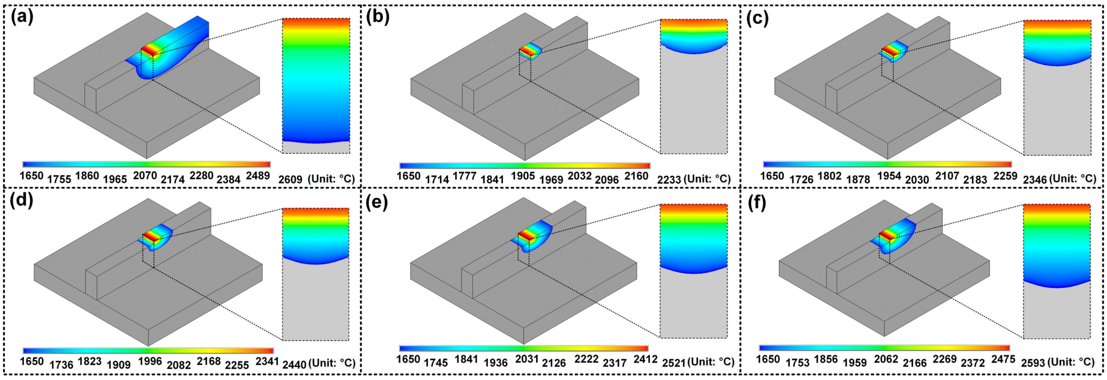

Fig. 6 Cloud map of the transient molten pool morphology of the LMAAM sample: (a) case1, (b) case2,(c) case3,(d) case4,(e) case5,(f) case5.

Fig. 7 showed the Temperature distribution of the LMAAM sample monitoring path and monitoring points. Observing Fig (a), it was found that the temperature distributions of the monitoring paths under different process parameters were similar, showing a distribution trend of high temperature in the central area and low temperature in both sides. If the slope of the curve at a certain position was used to characterize the temperature gradient of the monitoring path, it could be found that the areas with the largest temperature gradient in the monitoring path were concentrated on both sides of the sample and 1-2 mm from the top surface. The above position corresponded to the boundary position between the direct irradiation area and the non-direct irradiation area of the laser heat source, so there was a large temperature gradient in this area. At the same location of the monitoring path, the temperature of the sample with tin was lower and the temperature gradient was larger than that of the sample without tin. With the decrease of the distance between the tin liquid level and the top of the sample, the temperature at the corresponding position of the monitoring path decreased, and the temperature gradient decreased. Observing Fig (b), it was found that the thermal history curve of the monitoring point of the substrate showed a cyclical trend of first increasing and then decreasing, which corresponded to the process of each layer of coating deposited first and then condensed during the additive manufacturing process. With the movement of the laser, when the laser moved to or above the monitoring point, the temperature of the monitoring point increased, and when the laser beam left the monitoring point, the temperature of the monitoring point gradually decreased. The coating deposited first had a preheating effect on the coating deposited later, which made the peak temperature of the monitoring point of the substrate gradually increased during the additive manufacturing process. In the absence of tin, the peak temperature at the monitoring point was approximately similar at approximately 1600 °C as each coating was deposited. In the presence of tin, the peak temperature at the monitoring point decreased gradually with the deposition of the coating. It was worth noting that due to the hysteresis of heat transfer, the influence of tin on the temperature of the monitoring point of the substrate had a certain range, that was, the thermal sensitivity of the sample to tin had a certain threshold range. In the deposition process of the first two layers of coatings, the thermal history of the monitoring points of the substrate was slightly different. In the deposition process of the last eight layers, the effect of tin as a thermal management material on the additive sample was gradually revealed. With the increase of the distance between the tin liquid level and the top of the sample, the peak temperature of the monitoring point of the substrate gradually increased at the same moment of the additive process. And the thermal history curve of the monitoring point of the substrate gradually approached the thermal history curve of the sample without tin. Take the peak temperature corresponding to the last layer deposited as an example for analysis. When the distance between the tin liquid level and the top of the sample increased from 0.8 mm to 4.0 mm, the peak temperature increased from 1266 ℃ to 1530 ℃, and gradually approached the peak temperature (1645 ℃) corresponding to the sample without tin at the same time. Observing Fig. (c) and comparing Fig. (b), it was found that the curve morphology of the coating monitoring point and the substrate monitoring point were similar, and both showed a periodic change trend. Observation Fig. (c), it was found that the cooling rates of the samples were different under different conditions. The cooling rates of the samples under different conditions were calculated respectively. The peak cooling rate for the specimen without tin was 63.17 ℃/s(case1). The peak cooling rates of the samples with tin were 73.31 ℃/s(case2), 73.21 ℃/s(case3), 71.35 ℃/s(case4), 68.85 ℃/s(case5), 68.72 ℃/s(case6), respectively. The calculation results showed that the addition of tin could indeed increase the cooling rate of the sample. With the increase of the distance between the liquid level of tin and the top of the sample, the cooling rate of the sample decreased.

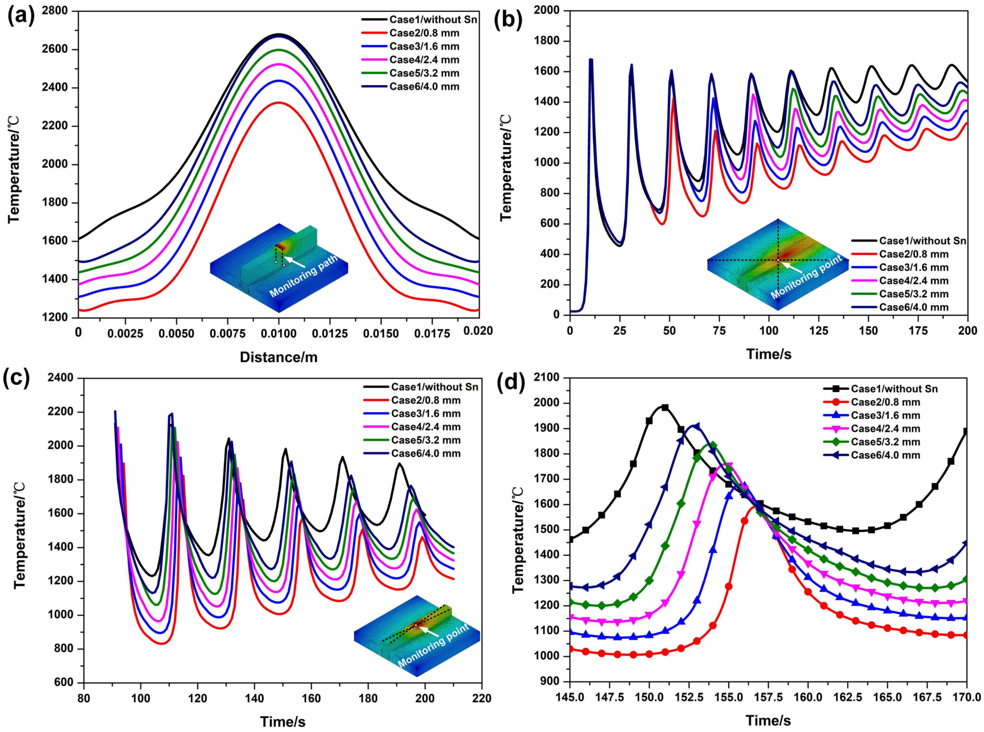

Fig. 7 Temperature distribution of the LMAAM sample monitoring path and monitoring points: (a) Temperature distribution curve of the monitoring path, (b) Thermal history curve of the first monitoring point, (c) Thermal history curve of the second monitoring point, (d) Local magnification of 145-170 s in the curve in Fig. (d).

4.3. Residual stress field analysis

Fig. 8 showed the cloud map of the transient thermal stress of LMAAM sample. The thermal stress distribution and numerical value in different regions of the sample were different. The tensile stress was concentrated in the coating area, and the other areas of the sample were under compressive stress. The tensile stress of the samples without tin was mainly distributed in the last coating. It was worth noting that after the addition of tin, the tensile stress distribution area of the sample gradually expanded from the last layer to the penultimate layer. With the increase of the distance between the tin liquid level and the top of the sample, the distribution area of tensile stress gradually increased. When the distance between the liquid level of tin and the top of the sample increased to 2.4 mm, the tensile stress of the sample did not change significantly. Compared with the sample without tin, the peak tensile stress of the sample with tin was larger, and with the increase of the distance between the tin liquid level and the top of the sample, the peak tensile stress of the sample increased gradually. The addition of tin made the heat exchange in different areas of the sample in contact with tin different, and there was more significant heat exchange below the liquid surface than above the liquid surface of tin. This undoubtedly increased the temperature gradient near the liquid surface. Under the multiple constraints of the material itself and the external environmental load, the thermal stress of the material increased.

Fig. 9 showed the cloud map of the residual stress of LMAAM sample. The residual stress distribution and numerical value of each part of the sample were different. The residual tensile stress was mainly distributed in the coating area. Compared to the samples without tin, the samples with tin had a reduced area of distribution of tensile stress, and the numerical value of the tensile stress was reduced. With the increase of the distance between the liquid level of tin and the top of the sample, the distribution area of the tensile stress of the sample gradually increased, and the tensile stress value gradually increased. The presence of tin would accelerate the heat transfer rate of the sample, increased the uniformity of the temperature distribution of the sample, and reduced the residual tensile stress. When the additive operation was over and the sample was cooled to room temperature, the interaction position between the liquid level of tin and the sample undoubtedly determined the residual stress distribution and value of the sample. The more areas the sample interacted with the tin, the lower the residual tensile stress of the sample.

Fig. 10 showed the thermal stress and residual stress distribution of LMAAM samples. The thermal stress at the monitoring point throughout the additive process was always compressive. It was worth noting that the addition of tin reduced the compressive stress at the monitoring point at the same time. And with the increase of the distance between the liquid level of tin and the top of the sample, the compressive stress at the monitoring point at the same time decreased gradually. For the same position of the sample, the increase of tensile stress would cause the decrease of compressive stress. Therefore, the addition of tin would make the tensile stress at the same position tend to increase. Compared with the sample without tin, the addition of tin in the additive manufacturing process would indeed reduce the residual tensile stress of the sample, but there were certain requirements for the amount of tin added. The distance between the tin level and the top of the sample should always be less than 2.4 mm. If it was higher than 2.4 mm, due to the insufficient heat exchange between tin and the sample, a large residual stress was induced.

The effect of liquid metal on the residual stress of the sample during additive manufacturing can be defined by the Zener-Wert-Avrami function[38], as shown in Eq. 28:

$$\frac{\sigma^{RS}}{\sigma_0^{RS}} = \exp[-(At_a)^m] \tag{28}$$

where σ_0^{RS} was the initial residual stress of the sample, σ^{RS} was the residual stress of the sample after heat treatment, t_a was the treatment time, and m was a numerical parameter that depended on the primary relaxation mechanism. A was represented by Eq.29:

$$A = B\exp\left[-\frac{\Delta H}{kT_a}\right] \tag{29}$$

where B was a constant, k was the Boltzmann constant, and ΔH was the activation heat of the thermal relaxation process. In this work, the values of variables σ_0^{RS} and t_a were constant, so σ^{RS} depended on T_a. Combining Eq. 1 and Eq. 2, σ^{RS} decreased with the increase of heat treatment temperature T_a until it reached a threshold value. The addition of liquid metal increased the preheating temperature of the additively manufactured samples, which had a certain effect of heat treatment, so it was beneficial to reduce the harmful residual tensile stress in the material and improve the mechanical properties of the material.

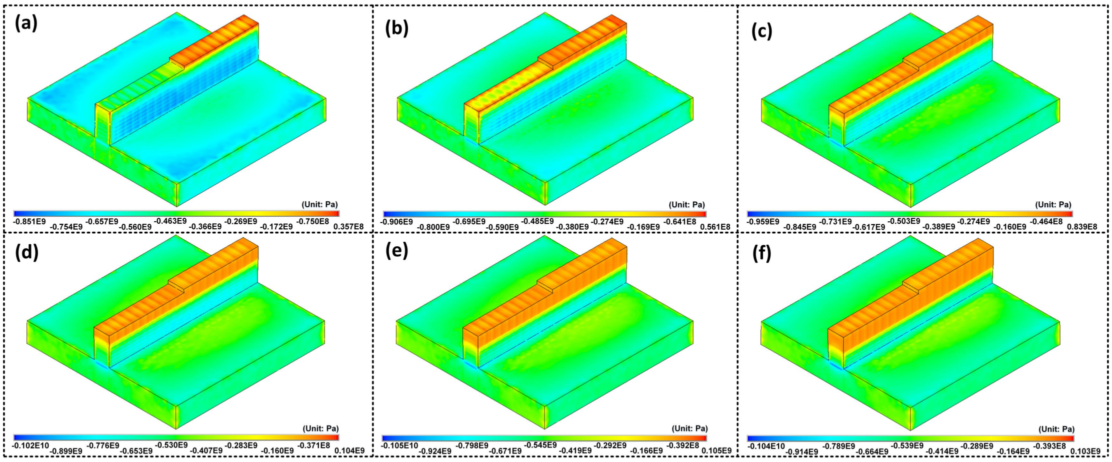

Fig. 8 Cloud map of the transient thermal stress of LMAAM sample: (a) case1, (b) case2,(c) case3,(d) case4,(e) case5,(f) case6.

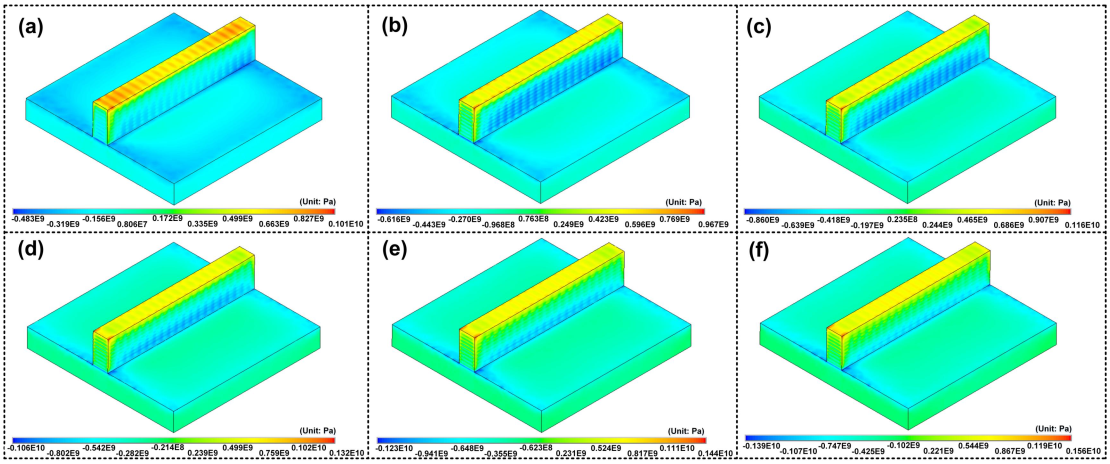

Fig. 9 Cloud map of the residual stress of LMAAM sample: (a) case1, (b) case2,(c) case3,(d) case4,(e) case5,(f) case5.

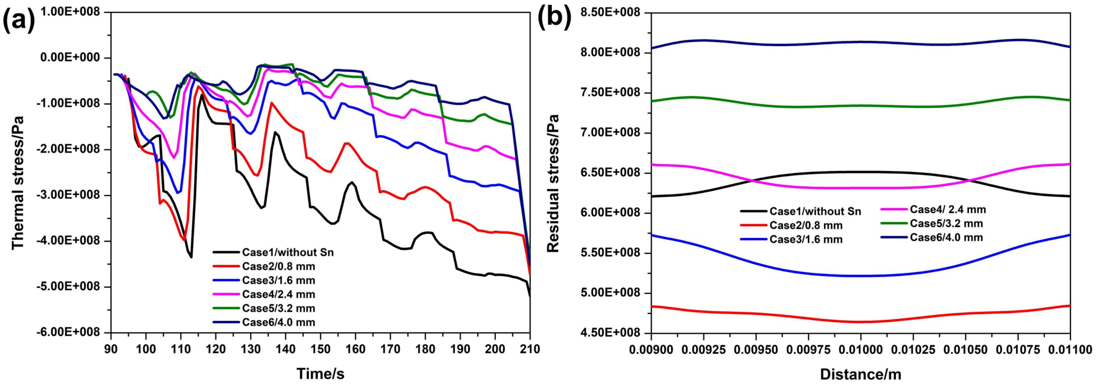

Fig. 10 Thermal stress and residual stress distribution of LMAAM samples: (a) Thermal stress history curve of monitoring point, (b) Residual stress curve of monitoring path.

5. Experiment results and discussion

5.1. Morphology analysis

Fig. 11 showed the morphology of the samples under different process conditions. Comparing Fig. 11(a) with Fig. 11(d), it was found that the deformation of the substrate of the sample without tin was larger than that of the sample with tin, and the substrate was warped. Comparing Fig. 11(b) with Fig. 11(e), and comparing Fig. 11(c) with Fig. 11(f), it could be found that the sample without tin had obvious crack defects and larger grain size. However, no obvious crack defects were observed in the samples with tin, and the grain size was relatively small. The EBSD test results can also further verify the refinement effect of liquid metal on the grain structure of the material. **Fig. 12** showed the EBSD results of the microstructure of the samples under different process conditions. Comparing Fig. 12(a) and Fig. 12(b), it was found that the grains of the material produced by tin-assisted additive operation were finer than that of the sample without tin. Comparing Fig. 12(c) and Fig. 12(d), it was found that the grain size of the sample without tin was concentrated at 200 μm, and the grain size of the sample with tin was concentrated at 150 μm. Due to the high thermal conductivity of tin, it was used as an auxiliary thermal management material for additive manufacturing. During the additive manufacturing process, the heat exchange between the sample and the outside world would be accelerated, and the uniformity of the heat distribution of the sample would be increased. At the same time, the harmful residual stress was reduced, the cooling rate was increased, and the grain structure was refined.

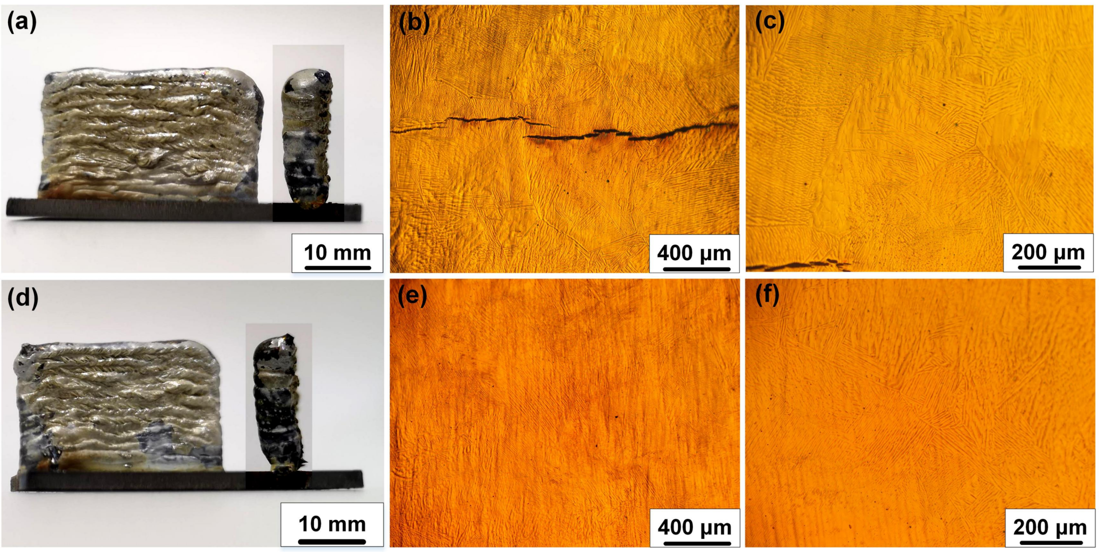

Fig. 11 Morphologies of the samples under different process conditions: (a) macro-morphology of the sample without tin, (b)-(c) micro-morphology of the sample without tin, (d) macro-morphology of the sample with tin, (e)-(f) Micromorphology of the samples with tin.

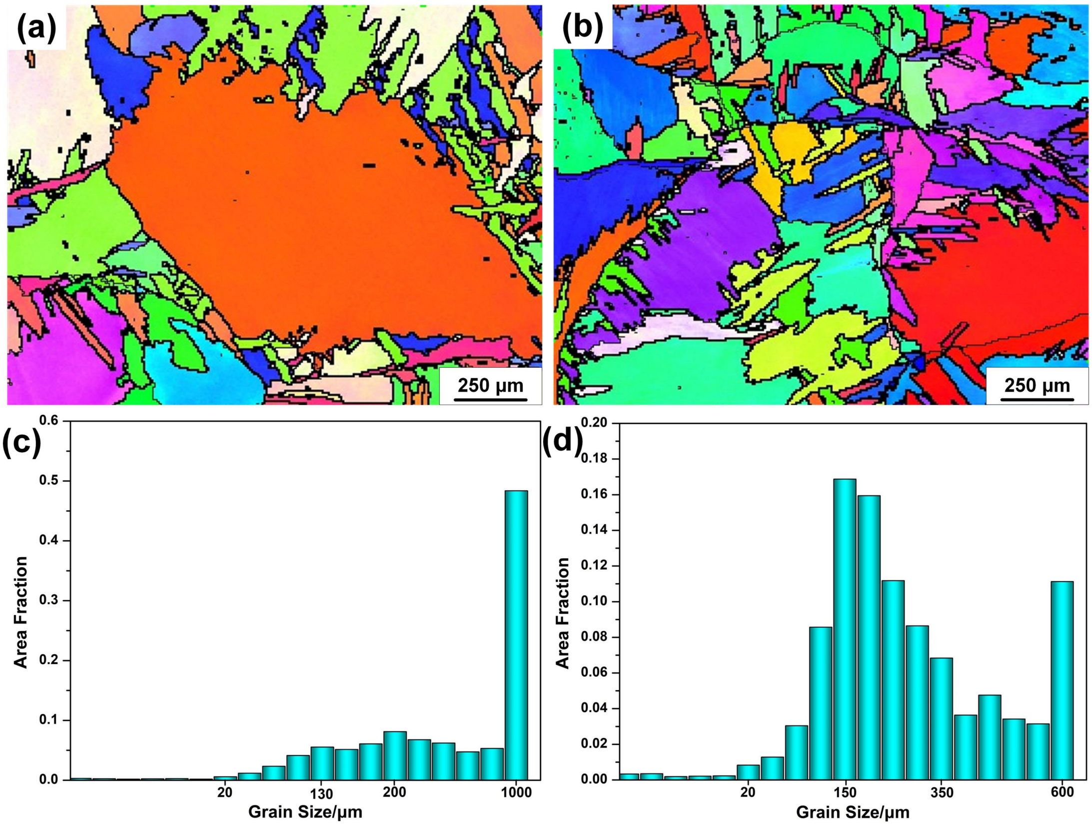

Fig. 12 EBSD results of the microstructure of the samples under different process conditions: (a) IPF image of the sample without tin, (b) IPF image of the sample with tin, (c) Statistical picture of the grain size distribution of the sample without tin, (d) Statistical picture of the grain size distribution of the sample with tin.

5.2. Online monitoring of LMAAM process

In the process of additive operation, there was an important relationship between the size of the molten pool and the heat transfer inside the molten pool. We acquired a series of time-lapse images of the melt pool of the samples with and without tin-assisted additive preparation with the aid of a high-speed camera, as shown in **Fig. 13**. In the laser additive manufacturing process, there were complex physical phenomena such as laser-material, laser-plasma interaction, etc. At the moment when the laser interacted with the material, the material absorbed the laser energy and was heated, which in turn caused the material to melt and evaporate, forming a transparent vapor, which was then ignited. As the laser energy continues to increase, the laser interacted with the material vapor on the surface of the material, resulting in a rapid increased in temperature and vapor ionization. When the ionization reached a certain level, the plasma was considered to be ignited. In addition, we could also observe obvious spatter, which was attributed to the silver-white oxide scale produced by chilling after the interaction of laser and matter (as shown in Fig. 8(a) and 8(d)). Compared with the samples without tin, the molten pool size of the samples with tin was smaller, which was attributed to the excellent heat transfer properties of tin, which accelerated the heat exchange between the samples and the outside world and increased the cooling rate.

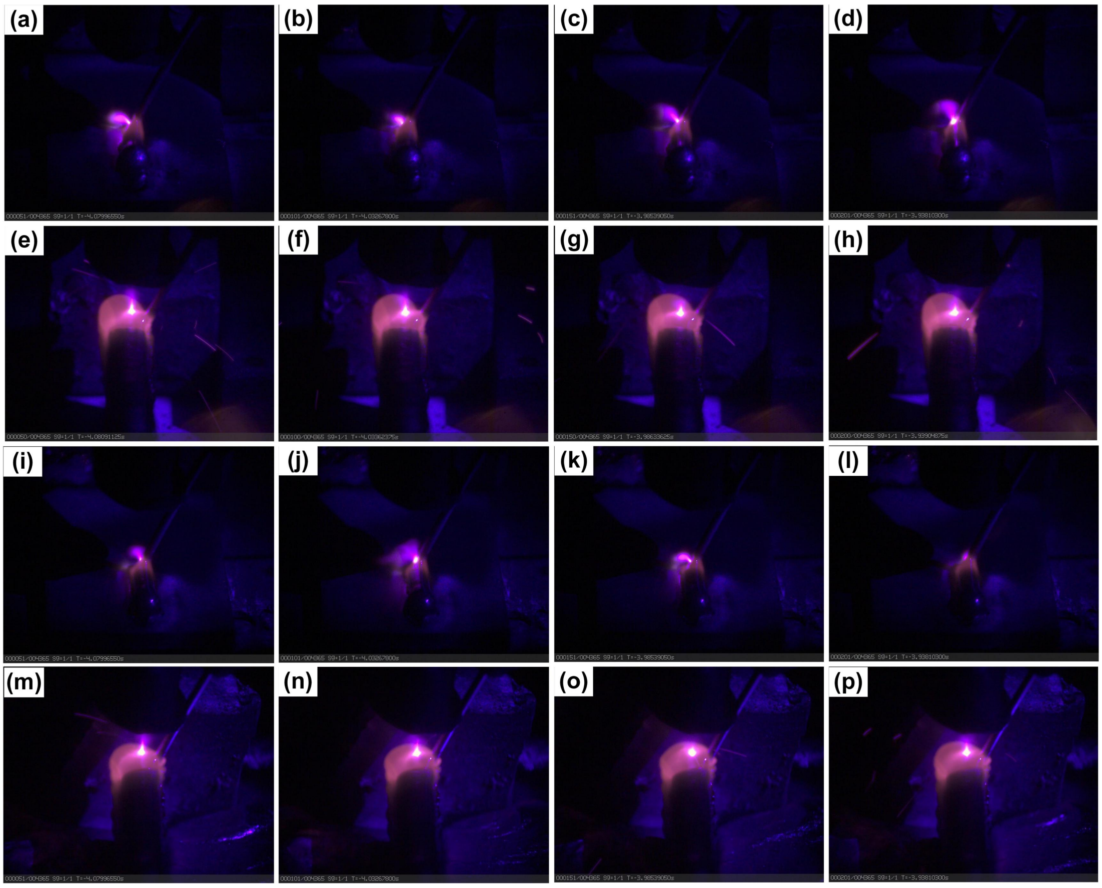

Fig. 13 Time-lapse images of samples without and with tin: (a)-(d) Additive layer 1/sample without tin, (e)-(h) Additive layer 10/sample without tin, (i)-(l) Additive layer 1/sample with tin, (m)-(p) Additive layer 10/sample with tin.

5.3. XRD and microhardness analysis

Fig. 14 showed the microhardness and XRD diffraction patterns of the samples under different process conditions. Observing Fig. 14(a), it was found that the microhardness of the samples with tin was higher than that of the samples produced by the additive operation without tin. The increase in sample hardness was attributed to the increase in material strength due to grain refinement. Observing Fig. 14(b), it was found that the diffraction peak intensity of the α phase of the sample with tin was higher than that of the sample without tin, which indicated that the sample produced by tin-assisted additive has more α phase. Due to the addition of tin, the cooling rate inside the molten pool during the additive operation was increased, the content of phase α increased, the residual tensile stress of the sample was reduced, and the diffraction peak appeared to shift to a high angle. The hardness of the material increased as the content of the A phase increased. At the same time, hardness was related to grain size. Liu et al.[39] proposed that microhardness was closely related to Hall-Petch theory and could be expressed by Hall-Petch theory, as shown in Eq. 30.

$$H = H_0 + k_h d^{-1/2} \tag{30}$$

where H was the hardness of the material, H_0 was the intrinsic hardness, k_h was the Hall-Petch coefficient, and d was the average grain size. It could be seen from Eq. 17 that the material hardness was inversely proportional to the grain size. The addition of liquid metal achieved a reduction in the grain size and therefore an increase in the microhardness.

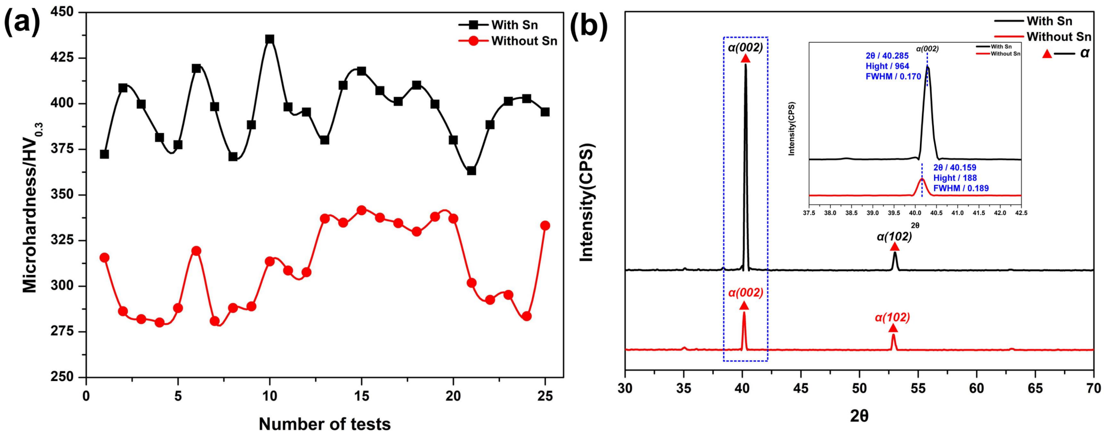

Fig. 14 Microhardness and XRD diffraction patterns of the samples under different process conditions: (a) Microhardness, (b) XRD diffraction pattern.

4. Conclusions

This work contributed a novel liquid metal-assisted laser additive manufacturing method. A numerical model for the laser additive manufacturing of tin-assisted titanium alloys was established. The validity of the model was verified experimentally to verify the thermal management properties of tin in additive manufacturing. During the additive process, the addition of tin increased the thermal stress of the sample, but reduced the detrimental residual stress of the sample. In addition, the addition of tin would increase the cooling rate of the sample, refine the grain structure, and improve the microhardness. As the distance between the liquid level of tin and the top of the sample decreased, the peak temperature of the sample decreased, the cooling rate increased, and the residual tensile stress decreased. It was expected that by adjusting the temperature of tin and the position where the liquid level of tin interacted with the sample, the thermodynamic control of the structure could be achieved, and then the microscopic morphology and even the mechanical properties of the structure could be controlled. In the process of additive manufacturing, there might be complex reaction mechanisms between tin and metal materials, which might be detrimental to formed parts. How to effectively suppressed the interaction between the thermal management material and the formed parts was also one of our main research work. We would discuss this issue in the next work.

Acknowledgements

This work was supported by the National Natural Science Foundation of China (Grant No. 51901162). The authors thanked the support of the Chinese National Talent Program.

References

[1] B. Zhang, S. Liu, Y.C. Shin, In-Process monitoring of porosity during laser additive manufacturing process, Addit. Manuf. 28 (2019) 497–505. https://doi.org/10.1016/j.addma.2019.05.030.

[2] A.G. Demir, B. Previtali, Additive manufacturing of cardiovascular CoCr stents by selective laser melting, Mater. Des. 119 (2017) 338–350. https://doi.org/10.1016/j.matdes.2017.01.091.

[3] A. Aramian, S.M.J. Razavi, Z. Sadeghian, F. Berto, A review of additive manufacturing of cermets, Addit. Manuf. 33 (2020) 101130. https://doi.org/10.1016/j.addma.2020.101130.

[4] B. Blakey-Milner, P. Gradl, G. Snedden, M. Brooks, J. Pitot, E. Lopez, M. Leary, F. Berto, A. du Plessis, Metal additive manufacturing in aerospace: A review, Mater. Des. 209 (2021) 110008. https://doi.org/10.1016/j.matdes.2021.110008.

[5] D. Herzog, V. Seyda, E. Wycisk, C. Emmelmann, Additive manufacturing of metals, Acta Mater. 117 (2016) 371–392. https://doi.org/10.1016/j.actamat.2016.07.019.

[6] D. Gu, C. Ma, M. Xia, D. Dai, Q. Shi, A Multiscale Understanding of the Thermodynamic and Kinetic Mechanisms of Laser Additive Manufacturing, Engineering. 3 (2017) 675–684. https://doi.org/10.1016/J.ENG.2017.05.011.

[7] L. Zhao, J.G. Santos Macías, A. Dolimont, A. Simar, E. Rivière-Lorphèvre, Comparison of residual stresses obtained by the crack compliance method for parts produced by different metal additive manufacturing techniques and after friction stir processing, Addit. Manuf. 36 (2020) 101499. https://doi.org/10.1016/j.addma.2020.101499.

[8] J. V. Gordon, C. V. Haden, H.F. Nied, R.P. Vinci, D.G. Harlow, Fatigue crack growth anisotropy, texture and residual stress in austenitic steel made by wire and arc additive manufacturing, Mater. Sci. Eng. A. 724 (2018) 431–438. https://doi.org/10.1016/j.msea.2018.03.075.

[9] K. Ha, T. Kim, G.Y. Baek, J.B. Jeon, D. sik Shim, Y.H. Moon, W. Lee, Numerical study of the effect of progressive solidification on residual stress in single-bead-on-plate additive manufacturing, Addit. Manuf. 34 (2020) 101245. https://doi.org/10.1016/j.addma.2020.101245.

[10] S. Chandra, X. Tan, R.L. Narayan, C. Wang, S.B. Tor, G. Seet, A generalised hot cracking criterion for nickel-based superalloys additively manufactured by electron beam melting, Addit. Manuf. 37 (2021) 101633. https://doi.org/10.1016/j.addma.2020.101633.

[11] G. Vastola, G. Zhang, Q.X. Pei, Y.W. Zhang, Controlling of residual stress in additive manufacturing of Ti6Al4V by finite element modeling, Addit. Manuf. 12 (2016) 231–239. https://doi.org/10.1016/j.addma.2016.05.010.

[12] T. Mukherjee, W. Zhang, T. DebRoy, An improved prediction of residual stresses and distortion in additive manufacturing, Comput. Mater. Sci. 126 (2017) 360–372. https://doi.org/10.1016/j.commatsci.2016.10.003.

[13] R. Li, G. Wang, X. Zhao, F. Dai, C. Huang, M. Zhang, X. Chen, H. Song, H. Zhang, Effect of path strategy on residual stress and distortion in laser and cold metal transfer hybrid additive manufacturing, Addit. Manuf. 46 (2021) 102203. https://doi.org/10.1016/j.addma.2021.102203.

[14] N.C. Levkulich, S.L. Semiatin, J.E. Gockel, J.R. Middendorf, A.T. DeWald, N.W. Klingbeil, The effect of process parameters on residual stress evolution and distortion in the laser powder bed fusion of Ti-6Al-4V, Addit. Manuf. 28 (2019) 475–484. https://doi.org/10.1016/j.addma.2019.05.015.

[15] C. Zhou, Q. Sun, D. Qian, J. Liu, J. Sun, Z. Sun, Effect of deep cryogenic treatment on mechanical properties and residual stress of AlSi10Mg alloy fabricated by laser powder bed fusion, J. Mater. Process. Technol. 303 (2022) 117543. https://doi.org/10.1016/j.jmatprotec.2022.117543.

[16] J. Zhou, X. Han, H. Li, S. Liu, J. Yi, Investigation of layer-by-layer laser remelting to improve surface quality, microstructure, and mechanical properties of laser powder bed fused AlSi10Mg alloy, Mater. Des. 210 (2021) 110092. https://doi.org/10.1016/j.matdes.2021.110092.

[17] Z. Tong, H. Liu, J. Jiao, W. Zhou, Y. Yang, X. Ren, Microstructure, microhardness and residual stress of laser additive manufactured CoCrFeMnNi high-entropy alloy subjected to laser shock peening, J. Mater. Process. Technol. 285 (2020) 116806. https://doi.org/10.1016/j.jmatprotec.2020.116806.

[18] J.R. Hönnige, P.A. Colegrove, S. Ganguly, E. Eimer, S. Kabra, S. Williams, Control of residual stress and distortion in aluminium wire + arc additive manufacture with rolling, Addit. Manuf. 22 (2018) 775–783. https://doi.org/10.1016/j.addma.2018.06.015.

[19] J.D. Roehling, W.L. Smith, T.T. Roehling, B. Vrancken, G.M. Guss, J.T. McKeown, M.R. Hill, M.J. Matthews, Reducing residual stress by selective large-area diode surface heating during laser powder bed fusion additive manufacturing, Addit. Manuf. 28 (2019) 228–235. https://doi.org/10.1016/j.addma.2019.05.009.

[20] H. Shen, J. Lin, Z. Zhou, B. Liu, Effect of induction heat treatment on residual stress distribution of components fabricated by wire arc additive manufacturing, J. Manuf. Process. 75 (2022) 331–345. https://doi.org/10.1016/j.jmapro.2022.01.018.

[21] X. Wei, X. Li, L. Zhang, Q. Lv, Effect of in-situ ultrasonic impact treatment on flow and solidification behavior of laser metal deposition: By finite element simulation, Int. J. Heat Mass Transf. 192 (2022) 122914. https://doi.org/10.1016/j.ijheatmasstransfer.2022.122914.

[22] W. Hackenhaar, J.A.E. Mazzaferro, F. Montevecchi, G. Campatelli, An experimental-numerical study of active cooling in wire arc additive manufacturing, J. Manuf.

Process. 52 (2020) 58–65. https://doi.org/10.1016/j.jmapro.2020.01.051.

[23] J. Nie, C. Chen, S. Shuai, X. Liu, R. Zhao, J. Wang, H. Liao, Z. Ren, Effect of Static Magnetic Field on the Evolution of Residual Stress and Microstructure of Laser Remelted Inconel 718 Superalloy, J. Therm. Spray Technol. 29 (2020) 1410–1423. https://doi.org/10.1007/s11666-020-01039-0.

[24] K. Kalantar-Zadeh, J. Tang, T. Daeneke, A.P. O'Mullane, L.A. Stewart, J. Liu, C. Majidi, R.S. Ruoff, P.S. Weiss, M.D. Dickey, Emergence of Liquid Metals in Nanotechnology, ACS Nano. 13 (2019) 7388–7395. https://doi.org/10.1021/acsnano.9b04843.

[25] B. Yuan, X. Sun, H. Wang, J. Liu, Liquid metal bubbles, Appl. Mater. Today. 24 (2021) 101151. https://doi.org/10.1016/j.apmt.2021.101151.

[26] G. Bo, L. Ren, X. Xu, Y. Du, S. Dou, Recent progress on liquid metals and their applications, Adv. Phys. X. 3 (2018) 412–442. https://doi.org/10.1080/23746149.2018.1446359.

[27] T. Daeneke, K. Khoshmanesh, N. Mahmood, I.A. De Castro, D. Esrafilzadeh, S.J. Barrow, M.D. Dickey, K. Kalantar-Zadeh, Liquid metals: Fundamentals and applications in chemistry, Chem. Soc. Rev. 47 (2018) 4073–4111. https://doi.org/10.1039/c7cs00043j.

[28] K. Zhao, Y.H. Ma, L.H. Lou, Improvement of creep rupture strength of a liquid metal cooling directionally solidified nickel-base superalloy by carbides, J. Alloys Compd. 475 (2009) 648–651. https://doi.org/10.1016/j.jallcom.2008.07.127.

[29] J. Shen, Z.G. Xu, Y.Z. Lu, W. Zheng, L.H. Lou, J. Zhang, Reaction of Ni-Based Superalloy with Liquid Sn During Liquid-Metal-Cooled Directional Solidification, Metall. Mater. Trans. A Phys. Metall. Mater. Sci. 49 (2018) 4003–4011. https://doi.org/10.1007/s11661-018-4758-1.

[30] W. Huang, H. Wang, T. Rinker, W. Tan, Investigation of metal mixing in laser keyhole welding of dissimilar metals, Mater. Des. 195 (2020) 109056. https://doi.org/10.1016/j.matdes.2020.109056.

[31] J.H. Cho, D.F. Farson, J.O. Milewski, K.J. Hollis, Weld pool flows during initial stages of keyhole formation in laser welding, J. Phys. D. Appl. Phys. 42 (2009). https://doi.org/10.1088/0022-3727/42/17/175502.

[32] R. Ammer, M. Markl, U. Ljungblad, C. Körner, U. Rüde, Simulating fast electron beam melting with a parallel thermal free surface lattice Boltzmann method, Comput. Math. with Appl. 67 (2014) 318–330. https://doi.org/10.1016/j.camwa.2013.10.001.

[33] C. Lampa, A.F.H. Kaplan, J. Powell, C. Magnusson, An analytical thermodynamic model of laser welding, J. Phys. D. Appl. Phys. 30 (1997) 1293–1299. https://doi.org/10.1088/0022-3727/30/9/004.

[34] H.S. Tran, J.T. Tchuindjang, H. Paydas, A. Mertens, R.T. Jardin, L. Duchêne, R. Carrus, J. Lecomte-Beckers, A.M. Habraken, 3D thermal finite element analysis of laser cladding processed Ti-6Al-4V part with microstructural correlations, Mater. Des. 128 (2017) 130–142. https://doi.org/10.1016/j.matdes.2017.04.092.

[35] X. Zhan, Y. Liu, W. Ou, C. Gu, Y. Wei, The Numerical and Experimental Investigation of the

Multi-layer Laser-MIG Hybrid Welding for Fe36Ni Invar Alloy, J. Mater. Eng. Perform. 24 (2015) 4948–4957. https://doi.org/10.1007/s11665-015-1808-3.

[36] G.F. Sun, Z.D. Wang, Y. Lu, R. Zhou, Z.H. Ni, X. Gu, Z.G. Wang, Numerical and experimental investigation of thermal field and residual stress in laser-MIG hybrid welded NV E690 steel plates, J. Manuf. Process. 34 (2018) 106–120. https://doi.org/10.1016/j.jmapro.2018.05.023.

[37] N. Shamsundar, E.M. Sparrow, Analysis of Multidimensional Conduction Phase Change Via the Enthalpy Model., Am. Soc. Mech. Eng. (1975) 333–340.

[38] D. Deng, R.L. Peng, H. Brodin, J. Moverare, Microstructure and mechanical properties of Inconel 718 produced by selective laser melting: Sample orientation dependence and effects of post heat treatments, Mater. Sci. Eng. A. 713 (2018) 294–306. https://doi.org/10.1016/j.msea.2017.12.043.

[39] W.H. Liu, Y. Wu, J.Y. He, T.G. Nieh, Z.P. Lu, Grain growth and the Hall-Petch relationship in a high-entropy FeCrNiCoMn alloy, Scr. Mater. 68 (2013) 526–529. https://doi.org/10.1016/j.scriptamat.2012.12.002.